IEEE Access
Multidisciplinary | Rapid Review | Open Access Journal

Received 22 June 2023, accepted 10 July 2023, date of publication 28 July 2023, date of current version 2 August 2023.

Digital Object Identifier 10.1109/ACCESS.2023.3299816

RESEARCH ARTICLE

Design Decisions for a Powertrain Combination of Electric Motor and Propeller for an Electric Aircraft

RALF JOHANNES KEUTER[1,2], (Graduate Student Member, IEEE), BASTIAN KIRSCH[1,3], JENS FRIEDRICHS[1,3], AND BERND PONICK[1,2]

[1]Cluster of Excellence SE[2]A–Sustainable and Energy-Efficient Aviation, Technische Universität Braunschweig, 38106 Braunschweig, Germany
[2]Institute for Drive Systems and Power Electronics, Leibniz University Hannover, 30167 Hannover, Germany
[3]Institute of Jet Propulsion and Turbomachinery, Technische Universität Braunschweig, 38106 Braunschweig, Germany

Corresponding author: Ralf Johannes Keuter (ralf.keuter@ial.uni-hannover.de)

This work was supported by the Deutsche Forschungsgemeinschaft (DFG, German Research Foundation) through the Germany's Excellence Strategy-EXC 2163/1-Sustainable and Energy Efficient Aviation under Project 390881007.

ABSTRACT For the sizing of an electric motor, the diameter and length of the installation space are important parameters that significantly influence and limit the characteristics of the electric motor. From an aerodynamic point of view, it is not technically advantageous to choose a propeller hub diameter that is larger than mechanically necessary. The hub diameter defines the installation space ans thus the outer diameter for the electric motor driving the propeller. The research question that arises is this: Is there an optimum diameter for the hub and thus the electric motor and how is it limited? The present work should help to establish a better understanding of the system combination of electric motor and propeller, especially the choice of the diameter and further geometrical parameters of the electric motor. A parameter study investigating aeromechanical and electromagnetic aspects has been performed and the results are combined to achieve the best solution in terms of efficiency and power density. The investigations show that an increase in the diameter causes little disadvantage from an aerodynamic point of view, but the improvements to the electric motor are significant only up to the point where the diameter-to-length ratio becomes too high and end-region effects become more significant. The installation space for the electric motor could be determined using a hub-to-tip ratio of 0.16 to 0.20, which is applicable to any propeller. In addition, it could be shown that a co-optimisation of the speed throughout a mission profile with regard to the efficiency is affected by the propeller alone.

INDEX TERMS Aviation, electric propulsion system, electric aircraft, permanent magnet synchronous motor, electrified aircraft propulsion, electric motor design, propeller design.

NOMENCLATURE

α'	Rotational interference factor.
β	Propeller pitch angle.
δ	Length of air gap.
$\dot{m}$	Massflow.
η	Efficiency.
γ'	Circumferential angle.
μ_0	Permeability constant.
ν	Hub-to-tip ratio.
Ω	Rotational speed of propeller.
ω	Induced swirl by propeller.
ϕ	Flow angle.
ρ_a	Density of air.
$\cos(\varphi)$	Power factor.
ϑ	Temperature.
A	Cross-section.
A	Electric loading.
a	Axial interference factor.
A_r	Propeller disk area.

The associate editor coordinating the review of this manuscript and approving it for publication was Kan Liu.

B	Magnetic flux density.
b	Width.
c	Chord length.
C_D	Drag coefficient.
C_L	Lift coefficient.
C_T	Thrust coefficient.
$D_{\mathrm{a},1}$	Outer stator diameter.
D_h	Hub diameter.
$D_{\mathrm{i},1}$	Inner stator diameter.
D_p	Propeller diameter.
F	Tip loss factor.
h	Heat transfer coefficient.
h	Height.
i	Split ratio.
I_1	Current.
i_ST	Ratio of tooth width to slot width.
i_TY	Ratio of tooth width to yoke height.
J	Current density.
k	Number of propulsion units.
k_cu	Copper filling factor.
k_m	Flux concentration factor.
L/D	Lift-to-drag ratio.
l_Fe	Motor stator core length.
M	Torque.
m	Mass.
n	Rotational speed.
P	Power.
q	Slots per pole and phase.
r	Radial distance to axis of rotation.
T	Thrust.
U	Voltage.
v	Velocity.
W	Gravimetric energy density.

ACRONYMS

AEA	All-Electric Aircraft.
BEMT	Blade Element Momentum Theory.
EASA	European Union Aviation Safety Agency.
PAX	Approximate Number of Passengers.
PMSM	Permanent Magnet Synchronous Motor.
PU	Propulsion Unit.

I. INTRODUCTION

The reduction of CO_2 and NO_x in aviation is becoming increasingly important. This can be seen in the emergence of many projects which share this goal. For wide-body long range aircraft, there is the possibility of improvement by increasing the bypass ratio of the turbofan engine. For commuter and regional aircraft, potential aerodynamic improvements exist in the use of distributed propulsion units (PU). These generate a maximum lift coefficient by providing substantially increased dynamic pressure across the wing at low speeds [1]. This so-called distributed propulsion approach can only be implemented in a technically advantageous way through the electrification of the PU. The benefits and challenges are discussed in [2]. One of the challenges is the need for high efficiency and high power density electric motors. Figure 1 shows the investigated aircraft, which is comparable to an ATR-72-600 in terms of its characteristics. The fundamental characteristics of this aircraft and the associated flight mission were developed in [3].

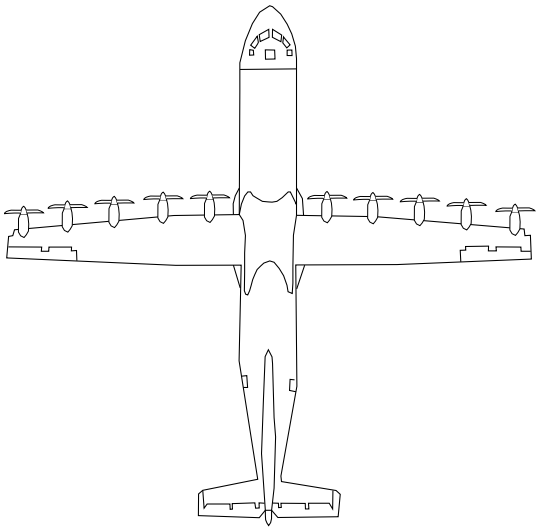

FIGURE 1. Sketch of the aircraft investigated with $k = 10$ distributed propulsion units.

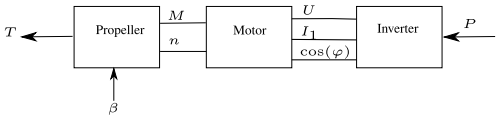

FIGURE 2. Interfaces between propeller and electric motor with regard to the operating strategy.

The pairing of propeller and electric motor raises the question of the holistic optimization potential offered by these components and of design decisions that lead to the best result in terms of efficiency and power density. From an aircraft point of view, the propeller is a component that must provide a certain thrust at different operating points. This thrust

$$T = C_\mathrm{T} \cdot \rho_a \cdot n^2 \cdot D_\mathrm{p}^4 \tag{1}$$

results from the geometrical properties, in particular the propeller diameter D_p, the blade geometry, which influences the thrust coefficient C_T, and the rotational speed n at which the propeller operates. Propellers with a larger diameter are equipped with blade pitch control. Therefore the efficiency can be optimized depending on speed and pitch angle β for each operating point. This leads to the first possibility for optimization. The joint optimization of the overall efficiency of electric motor and propeller depends on the operating points of the flight mission.

The electric motor supplies the propeller with the necessary speed and torque which result in the required motor power

$$P = 2\pi \cdot M \cdot n. \tag{2}$$

For the electric motor, the installation space is crucial since it has a large impact on the torque generation. This

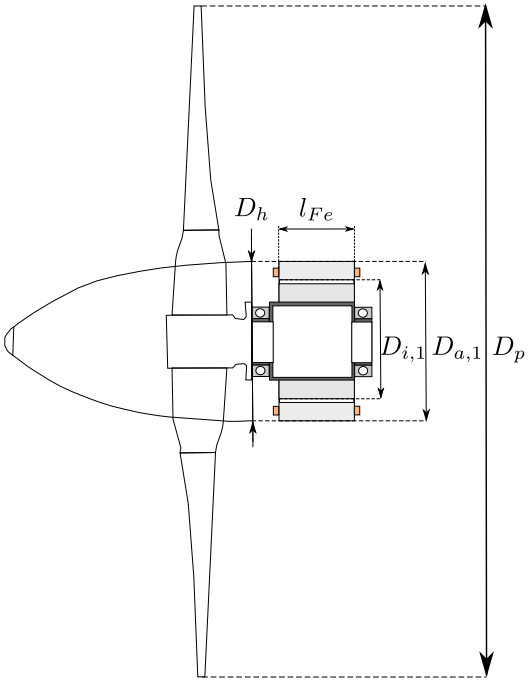

FIGURE 3. Interfaces between propeller and electric motor showing the geometry.

becomes particularly evident in Equation (20). The electric motor should not be larger in diameter than the hub; otherwise it will extend into the airflow of the propeller. The hub diameter does not have a major influence on the performance of the propeller if it is increased slightly. This results in the second possibility for optimization: the enlargement of the hub diameter. Figure 3 shows a sketch of the installation space of the electric motor. If the power of the electric motor is kept approximately constant, increasing the diameter $D_{\mathrm{a},1}$ will result in a shorter core length l_{Fe}. This leads to the end region effects, namely resistance and leakage inductance of the end winding and leakage flux of the permanent magnets, having a stronger influence and the advantages decreasing.

This publication has the purpose of giving insight into state-of-the-art combined propeller-motor optimization and operation strategy. In addition, reference values and advice on the design of an electrical machine with direct liquid conductor cooling are given.

II. STATE OF THE ART

The research fields of turbomachinery and electric motors have few interfaces; accordingly, there are few papers in which experts from both research fields come together. However, due to the efforts towards electrification of aircraft propulsion units, studies on the respective electric motors, propellers, fans, and their interaction can now be found.

Many studies consider the electric motor or the propeller as an isolated component. In [4], the benefits of the electric motor and propeller regarding the take-off noise were examined and a reduction of 12 dBA was achieved due to lower rotational speed, but a design of the electric motor as well as in [5] was not presented. In [6], an optimization method for a propeller-based propulsion system was explained.

For electric motors, aviation-specific aspects such as thermal management, multiphase systems, and power density are often addressed. In [7], an electric motor for a small aircraft was designed based on the power requirement, while in [8], a focus was set on the thermal design but the study made use of a measured flight mission with variable rotational speed. In most investigations, the propeller was considered only in the form of a given power and rotational speed. A design at 360 kW and a rotational speed of 6000 1/min was discussed in [9], with a focus on fault tolerance and the increase of power density with the help of a Halbach array. An interesting design which only considers power (500 kW) and rotational speed (3000 1/min) was shown in [10] using a an indirectly cooled approach with litz wire. The advantage of an electric motor with a large diameter and its better utilization of the copper material was discussed in [11], but the propeller was not considered in detail.

Since the overall efficiency plays an important role, a method for thrust control of a system consisting of an electric motor and a propeller was presented in [12]. The operating points of such a propulsion system with a fixed-bladed propeller were optimized in [13] and the result was 10% less energy consumption. A complete system with the focus on modeling the thermal system (nacelle, air intake, propeller) was shown in [8]. Design trade-offs for reducing acoustic noise, increasing aerodynamic efficiency and reducing the energy comsumption are shown in an investigation looking at the electric motor and the propeller [14]. The study [15] thus shows a whole system, but the focus of this work is the aircraft performance. An open source program for the calculation of propellers called XROTOR was used here. The design of the electric motor is not explained in detail.

In [16], a regional aircraft with a power of 40 MW was considered. The design of the ducted fan and electric motor was presented. The advantages of co-optimization were recognized here and demonstrated in a subsequent study [17], in which, among other things, the hub-to-tip ratio and the number of propellers were varied. The detailed influence of the respective components was not presented here. However, this work is the most sophisticated work yet considering the electric motor diameter as determined by the hub-to-tip ratio of the propeller.

III. MODELING OF PROPELLER AND PERFORMANCE EVALUATION

A. PROPELLER DESIGN METHOD

In this paper, the propeller is designed and calculated using the blade element momentum method. The method is presented in [18] and shown with all assumptions made. In this section, the governing equations will be briefly shown. The blade element momentum method used can be divided into two independent theories: the momentum theory and the blade element theory. In the overarching combined theory, it is assumed that the calculated forces of the two theories

agree. This must, in particular, apply to the thrust as well as to the torque. The thrust in momentum theory can be described by

$$T = \dot{m}\Delta v = \dot{m}(v_s - v_0). \tag{3}$$

Here, the propeller is modeled as a simple actuator disk. According to Newton's third law ''actio = reactio'', an acceleration of the flow between the slipstream s and the flow in front of the propeller 0 must occur due to the thrust T of the propeller. If it is then further assumed that the mass flow $\dot{m}$ through the propeller disk A_r does not mix with the surrounding air (conservation of mass), the thrust can be described by

$$T = A_r \rho_a v_0 (1 + a) 2\, v_0\, a. \tag{4}$$

where ρ_a represents the air density. The factor a is described as the axial interference factor and represents the velocity increase in front of the propeller. Neglecting losses, the power can be written as the change in kinetic energy between the inflow and slipstream

$$P = \frac{\dot{m}}{2}(v_s^2 - v_0^2) = v_r T = v_0(1 + a)T. \tag{5}$$

To account for the rotation of the propeller and the induced swirl in the flow field, the rotational interference factor a' is introduced as

$$a' = \frac{\omega}{2\Omega}. \tag{6}$$

This relates the rotational speed of the flow ω to the rotational speed of the propeller Ω. By dividing the rotor area into independent rings of width dr and distance r from the axis of rotation, the torque can finally be obtained as

$$dM = 4\pi r^3 dr\, \rho_a v_0 (1 + a)\Omega a'. \tag{7}$$

The equations shown so far apply to the momentum theory. The blade element method, however, considers the propeller blade as a series of independent wing elements with width dr. According to the flow around these elements, forces are generated which can be calculated using wing theory. Thus, if the speed of the flow at the blade element is v_{rel}, a lift force dL and a drag force dD are generated. These are connected via the flow angle ϕ to the thrust dT and the circumferential force dC by

$$dT = dL\cos(\phi) - dD\sin(\phi) \tag{8}$$

$$dC = dL\sin(\phi) + dD\cos(\phi). \tag{9}$$

Here, the flow angle ϕ is the angle between the axial velocity v_0 and relative velocity v_{rel} of the blade element. The total thrust and torque can finally be obtained by integration and multiplication by the number of blades N giving

$$T = N \int_{r_{hub}}^{r_{tip}} dT \tag{10}$$

$$M = N \int_{r_{hub}}^{r_{tip}} r dC. \tag{11}$$

The aforementioned requirement of equality of forces derived using the momentum theory and blade element theory leads to

$$4\pi r \rho_a v_0 (1 + a) v_0 a F = \frac{1}{2}\rho_a v_{rel}^2 c C_y \tag{12}$$

$$4\pi r^2 \rho_a v_0 (1 + a)\Omega a' F = \frac{1}{2}\rho_a v_{rel}^2 c C_x. \tag{13}$$

The relative velocity v_{rel} is composed of the superposition of axial and rotational velocity, including the interference factors, resulting in

$$v_{rel} = \sqrt{(v_0(1 + a))^2 + (\Omega r(1 - a'))^2} \tag{14}$$

c corresponds to the local chord length of the blade element. C_x and C_y relate to the aerodynamic coefficients for lift and drag as

$$C_y = C_L\cos(\phi) - C_D\sin(\phi) \tag{15}$$

$$C_x = C_L\sin(\phi) + C_D\cos(\phi). \tag{16}$$

The factor F appearing in equations 12 and 13 is called the Prandtl tip loss factor and models the loss due to the blade tip vortex. Based on these equations, an iterative design procedure and a calculation procedure for a propeller can be derived. The algorithm used in this paper is described in detail in [19]. The input variables are airspeed, rotational speed, flight altitude, tip diameter, hub diameter, the airfoils along the propeller with an associated lift distribution and a thrust requirement. These data determine the design of the propeller, which consists of chord length and blade angle for different radii from hub to tip. Thus, the geometry of the propeller is given and can be used to calculate its performance under varying operating conditions. These are described by the parameters axial speed v_0, rotational speed n, pitch angle β and height h. Since the first two parameters v_0 and n have a direct influence on the effective inflow velocity at the propeller blade, it is understandable that the forces change with them. The pitch angle β additionally allows the rotation of the propeller blade about an axis and thus influences the angle of attack of the propeller blade relative to the flow. This allows the propeller blade to be directly adjusted to suit changing inflow conditions and so to continue to operate at the optimum point. Finally, the flight altitude has an influence on the resulting forces on the propeller blade: The aerodynamic coefficients of the airfoils used change due to the changed air density and viscosity, since the coefficients are generally functions of the Reynolds number and the Mach number. If all these influences are taken into account, the dependencies of thrust T and power P arise as

$$T = f(v_0, n, \beta, h) \tag{17}$$

$$P = f(v_0, n, \beta, h). \tag{18}$$

TABLE 1. Characteristics of propeller designs with different hub diameters at cruise speed.

Case	Hub diameter in m	Power in kW	Efficiency in %	Relative pitch angle in deg
1	0.14	153.35	88.62	3.9303
2	0.1678	153.33	88.63	4.0499
3	0.1956	153.44	88.57	4.1812
4	0.2232	153.54	88.51	4.3205
5	0.251	153.66	88.44	4.4690
6	0.2788	153.78	88.38	4.6277
7	0.3066	153.90	88.30	4.7980
8	0.3342	154.03	88.23	4.9812
9	0.362	154.17	88.15	5.1788
10	0.3898	154.32	88.07	5.3932
11	0.4176	154.48	87.98	5.6261
12	0.4454	154.64	87.89	5.8792

Thus, the efficiency depends as well on these four factors, since

$$\eta_{prop} = \frac{Tv_0}{P} \tag{19}$$

applies.

B. PROPELLER DESIGN

The methods explained previously will now be applied to a concrete example. This is a propulsion unit consisting of electric motor and propeller for an aircraft with distributed propulsion with 10 identical propulsion units distributed at the wing. The mission requirements (see following section) are direct input variables for the design of the propeller. During the investigations, it was ensured that all requirements were met. For the design of the propeller, the blade element momentum theory (BEMT) was used. The propeller designed has an outer diameter of 1.5 m and a hub diameter of 0.14 m in the unadjusted reference version. This reference is assumed to be a classic propeller design and reflects the hub-to-tip ratio of a conventionally powered aircraft. At the cruise operating point studied, this propeller delivers a thrust of 950.6 N at 2650 1/min at an altitude of 6000 m. The speed is chosen so that a helical Mach number at the tip of the propeller of 0.8 is not exceeded. This also avoids creating supersonic regions, which significantly increase noise. All designs derived from this reference version have identical requirements and geometries. Thus, the first case is identical to the reference. Only the hub diameter varies from 0.14 m to 0.4454 m. Thus, a total of 12 propeller designs are available with varying hub-to-tip ratios from 0.093 to 0.297 with identical blade geometry above the hub diameter. All propellers were calculated after their design using different operating conditions. Tab. 1 lists their characteristics in cruise.

As can be seen from the data, the differences in performance and efficiency are very small. The pitching of the propeller blade counteracts the removal of the propeller blade area with comparatively very low aerodynamic losses. From an aerodynamic point of view, the same thrust is required from all the above designs. However, by shortening the blade height, the effective blade height that can generate the required thrust is reduced. This results in the propeller blade having a higher loading as the inner diameter increases. For the individual sections as defined in the BEMT, this means that they must generate higher forces. Since the inflow conditions (axial velocity, rotational speed, altitude) are identical for all propellers, the only way to achieve the required force is to vary the pitch angle and thus the angle of attack. However, not only the lift coefficient but also the drag coefficient of the respective position is changed at the same time. The two variables change independently of each other, so that their ratio also changes. It is therefore easy to see that the efficiency of the positions must also change and, as a consequence, so does the efficiency of the overall blade.

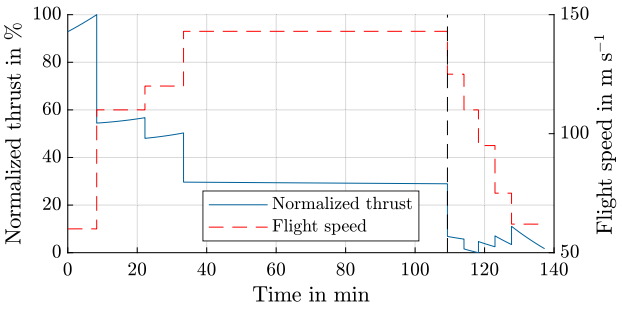

FIGURE 4. Propeller thrust and flight velocity during reference mission.

C. EVALUATION OF PROPELLER PERFORMANCE FOR REFERENCE MISSION

The reference mission used is a typical mission of a short-range aircraft. Figure 4 shows the thrust requirement of the propeller and the flight speed over the mission duration. This can be roughly divided into five segments: takeoff, climb, cruise, descent and landing. Sizing for the propeller in the present case is primarily determined by the conditions in the takeoff and climb segments. In the case of takeoff, high thrust is required at low flight speeds, which can only be achieved by a comparatively high rotational speed. At the same time, however, the speed is limited by the helical tip Mach number of 0.8 to avoid shockwaves. In the climb segment, this Mach number is also limiting. Here, the airspeed is about twice as high as in the takeoff case, which means that the propeller rotational speed must decrease. Nevertheless, the thrust requirement is about 55% of the maximum thrust. In this study, however, the focus is on the first three mission segments, namely takeoff, climb, and cruise. These segments are seen as determining the overall mission total energy requirements. Thus, the mission period under consideration ends with the end of the cruise segment, which is indicated by the dashed line in Figure 4.

If all 12 propellers are evaluated using the mission profile, there are is infinite number of solutions for each mission point with a thrust requirement at a given airspeed and altitude, due to the combination of rotational speed and pitch angle. The requirement for maximum efficiency at each mission point can be used as an additional constraint. This determines

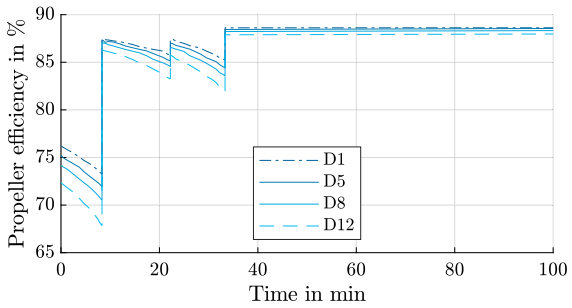

FIGURE 5. Propeller efficiency with varying hub diameter during reference mission.

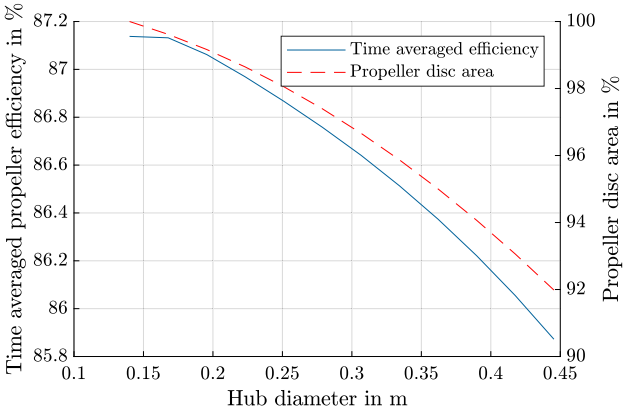

FIGURE 6. Time-averaged propeller efficiency during reference mission.

the rotational speed and therefore the pitch angle. Thus, the operating point of the propeller is uniquely determined. Figure 5 shows the efficiency of the propeller evaluated according to this scheme at some hub diameters according to Table 1.

It can be clearly seen that, in the highly loaded flight sections, the efficiency of the propeller decreases with increasing hub diameter. This is due to the same effect as described in the previous section: Due to the lower blade height, the propeller blade has a higher loading, which leads to an increase in the drag of the blade and thus also to an increase in the required power. In a further step, the efficiency can be averaged over the mission duration. This is included for all hub diameters in Figure 6.

The figure shows that the reference propeller with the smallest hub diameter achieves the highest efficiency. However, this maximum is comparatively low, with a difference of 1.26% from the largest hub diameter if it is taken into account in the same comparison that the propeller disc area decreases by 8%. The propeller disc area related to the reference diameter D1 is shown as the second curve in Figure 6 above. The two curves run very similarly in this study, so that a linear relationship can be assumed. However, it should be noted that the changes shown are dependent on the design of the propeller and cannot be generalized. The trends should nevertheless be similar for other propeller designs.

IV. FUNDAMENTALS OF ELECTRIC MOTOR DESIGN AND PARAMETER STUDY

Equation 2 shows that the motor delivers a certain torque M and rotational speed n to the propeller. A high-torque approach was chosen for the investigations because increasing the speed would require a gearbox, which would reduce overall efficiency, reduce reliability and increase complexity.

The torque

$$M(t) = l_{\mathrm{Fe}} \cdot \left(\frac{D_{\mathrm{i},1}}{2}\right)^2 \int_0^{2\pi} B(\gamma', t) \cdot A(\gamma', t)\ d\gamma' \qquad (20)$$

can be described based on Jordan's spatial harmonic theory [20] by the interaction of the electric loading $A(\gamma', t)$ and the flux density $B(\gamma', t)$ in the air gap of the electric motor. The equation also shows that the same torque can be generated from different combinations of active length l_{Fe} and inner stator diameter $D_{\mathrm{i},1}$. Because of the quadratic influence, it is advantageous to choose the inner diameter as large as possible. The outer diameter $D_{\mathrm{a},1}$ in this configuration was set depending on the propeller diameter D_{p}, as shown in Figure. 3. The relationship between these can be described by the hub-to-tip ratio ν. The influence of the inner diameter gives rise to an optimum for a fixed outer diameter in terms of the maximum torque, as explained in [21], where the author derives the analytical approximation for the torque

$$M \sim D_{\mathrm{i},1}^2 \cdot A \sim D_{\mathrm{i},1} \cdot D_{\mathrm{a},1}^2 - D_{\mathrm{i},1}^3 \qquad (21)$$

involving the inner diameter $D_{\mathrm{i},1}$ and electric loading A. Also, for the design of directly-liquid-cooled electric motors, the importance of the split ratio was identified and described as a sizing rule [22]. Therefore the split ratio

$$i = \frac{D_{\mathrm{i},1}}{D_{\mathrm{a},1}} \qquad (22)$$

was determined as the most important geometric sizing parameter beside the outer diameter. However, the analytical equation only serves as a theoretical construct which shows the existence of a pronounced optimum, which is also confirmed in the FEM (Fig. 12). The increase of the inner diameter and thus split ratio is supported by a higher number of pole pairs. This results in particular from the fact that the yoke can be made thinner. However, the yoke must have a sufficient cross-section to conduct the magnetic flux. This also applies to the tooth. In high utilized electrical motors, there is a trade-off between increasing the flux due to larger iron cross-sections (yoke and tooth) and increasing the stator leakage flux across the slot as shown in [23].

A. STATOR BOUNDARY CONDITIONS AND SIZING

Within the scope of this investigation, the slot geometry and the number of pole pairs p were adjusted in addition to the stator outer and inner diameters. With a fixed outer diameter, the inner diameter, tooth width b_{T} and yoke height h_{Y} were varied. Using the split ratio i, the impact of the ratio of tooth width to slot width

$$i_{\mathrm{ST}} = \frac{b_{\mathrm{T}}}{b_{\mathrm{S}}} \qquad (23)$$

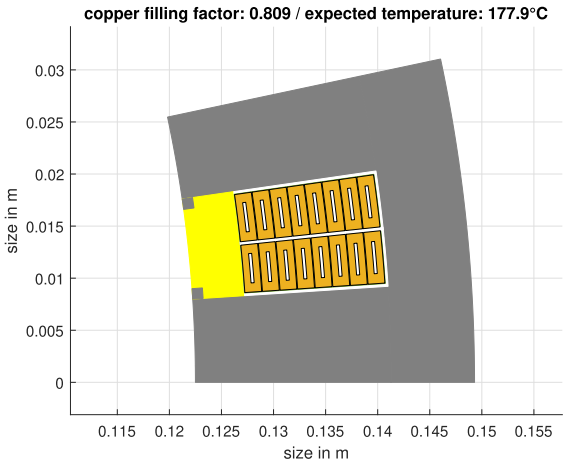

FIGURE 7. Conductor design of one slot of the fractional-slot concentrated winding with cooling channels used for direct liquid cooling of the coils.

and the ratio of yoke height to tooth width

$$i_{\mathrm{TY}} = \frac{h_{\mathrm{Y}}}{b_{\mathrm{T}}} \tag{24}$$

are evaluated.

With increasing diameter, larger numbers of pole pairs are necessary to create a reasonable geometry in combination with a spoke-type magnet rotor. A measure to set the number of pole pairs is the pole pitch; this was selected to be in the range of $\tau_{\mathrm{p}} \in [20\ 80]$ mm. The initial geometry for the parameter variation at each outer diameter was set up with $i_{\mathrm{TY}} = 1$.

B. WINDING AND COOLING DESIGN

The goal of high power density electric motors can be achieved by using directly-liquid-cooled coils. High current densities can be realized without exceeding the thermal limits [24]. These high current densities help to generate a high magnetomotive force from a smaller cross-section provided for the conductor. Beside the current density, it is important to look at the copper filling factor k_{Cu} since it influences significantly the ohmic resistance and therefore the joule losses,

$$J = \frac{I_1}{k_{\mathrm{Cu}} \cdot A_{\mathrm{S}}}. \tag{25}$$

The copper filling factor is defined by the total cross-section of the slot A_{S} and the total copper cross-section A_{Cu}. Therefore, the areas occupied by insulation and especially by the cooling channels have an impact. The winding was arranged as a fractional-slot concentrated winding with a number of slots per pole and phase of $q = \frac{2}{5}$, as shown in Fig 7.

In order to select a total cooling area only as large as necessary, the cooling channel cross-sectional area was iteratively increased until thermal equilibrium was reached

TABLE 2. Overview of the motor design constraints.

Parameter	Definition	Comment
P_{max}	270 kW	Take-off power
n_{max}	3100 min^{-1}	Maximum rotational speed
$D_{\mathrm{a},1}$	132 to 437.4 mm	Defined by propeller hub
$D_{\mathrm{i},1}$	variable	Object of investigation
l_{Fe}	variable	Adapted to power requirement
b_{T}	> 8 mm	Object of investigation
h_{Y}	> 8 mm	Object of investigation
δ	1.5 mm	Fixed setting
τ_{p}	20 to 80 mm	Dependent on p
J	60 $\mathrm{A/mm}^2$	Fixed setting
q	$2/5$	Fixed setting
k_{Cu}	$k_{\mathrm{Cu}}(A_{\mathrm{Cool}})$	Defined by cooling channels
Rotor topology	spoke-type magnets	Fixed setting
k_{m}	1.25	Fixed setting

at about 180 °C after solving the equations

$$h = \frac{P_{\mathrm{v,Cu}}}{A_{\mathrm{cool}} \cdot \Delta\vartheta_{\mathrm{ln}}} \tag{26}$$

$$\Delta\vartheta_{\mathrm{ln}} = \frac{\vartheta_{\mathrm{in}} - \vartheta_{\mathrm{out}}}{\ln \frac{\vartheta_{\mathrm{cond}} - \vartheta_{\mathrm{in}}}{\vartheta_{\mathrm{cond}} - \vartheta_{\mathrm{out}}}} \tag{27}$$

for the conductor temperature $\vartheta_{\mathrm{cond}}$ at the maximum power requirement. The heat transfer coefficient was chosen to be $h = 2500\ \mathrm{W/m^2K}$.

C. ROTOR

A spoke-type magnet arrangement was chosen as the rotor topology because it offers the twin advantages of high flux density and good protection against demagnetization. However, the rotor was not optimized specifically for the individual models, but rather across a range with a flux concentration factor $k_{\mathrm{m}} = 1.25$. The flux concentration factor is defined as

$$k_{\mathrm{m}} = \frac{2h_{\mathrm{m}}}{\tau_{\mathrm{p}}}, \tag{28}$$

as explained in [25] with the magnet height h_{m} and the pole pitch τ_{p}. In Tab. 2, an overview of the different parameters in this study is presented.

V. ELECTRIC MOTOR AND PROPELLER SPEED OPTIMIZED FLIGHT MISSION

The co-optimization of propeller and electrical machine for maximum efficiency with regard to the rotational speed during the flight mission is shown in Fig. 8. The graph shows that there are speed differences for the models D1 when only the propeller is optimized. This is due to the fact that the motor D1 has a lower efficiency and therefore has a larger influence on the optimisation. The higher the efficiency of the electrical machine, the lower its influence on the speed profile during a flight mission. This can be seen in the comparison of the models of propeller and motor D5, where the speed difference between the single propeller optimization and the co-optimization is nearly zero. From this, it can be concluded that the speed optimization can be carried out without the data concerning the electrical machine.

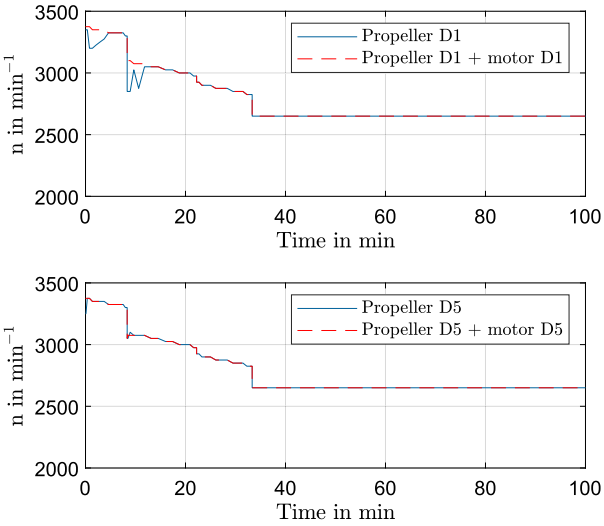

FIGURE 8. Comparison of the rotational speed optimized for maximum efficiency.

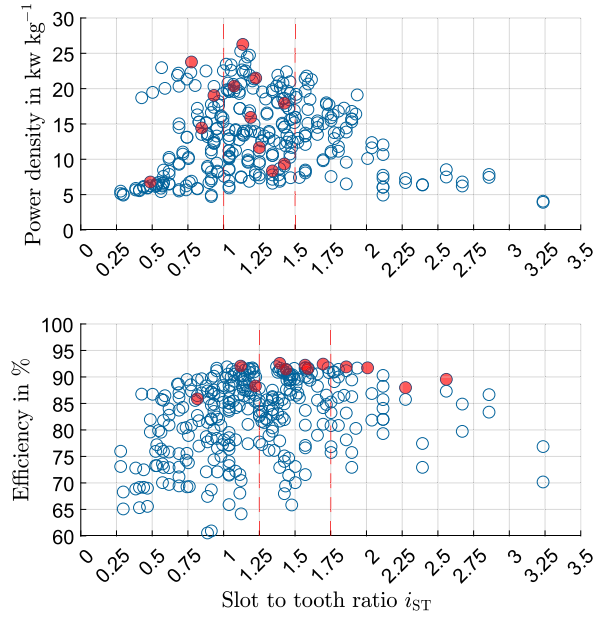

FIGURE 9. Impact of the ratio of tooth width to slot width i_{ST} on the power density and efficiency. The red dots show the maximum power density and efficiency at the corresponding diameter.

VI. ELECTRIC MOTOR PARAMETER STUDY AND EVALUATION

This section shows the influence of various parameters on power density and efficiency. Particularly noteworthy is the influence of the split ratio and the stronger influence of the end-region field with a short active length. The ratio of tooth width to slot width i_{ST} defines firstly the cross-section of the slot that generates the magnetomotive force with a fixed current density, and secondly the flux density in the tooth. The investigation shows that a value of i_{ST} between 0.9 to 1.5 leads to higher power densities because of the higher magnetomotive forces made possible by the larger slot cross-section. A value between 1.25 and 1.75 seems reasonable for higher efficiency. Figure 9 gives an overview.

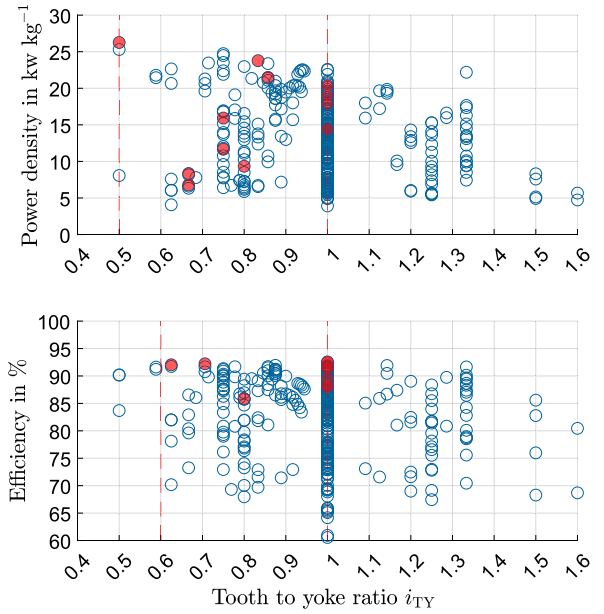

FIGURE 10. Impact of the ratio of tooth width to yoke height i_{TY} on the power density and efficiency. The red dots show the maximum power density and efficiency at the corresponding diameter.

The ratio of tooth width to yoke height i_{TY} affects the slot cross-section to a smaller extent, yet determines the flux density in the yoke area. It seems advantageous to set this ratio in the range of 0.5 to 1.0. This means that the yoke is half as high as the width of the tooth, or both have the same dimension. The results are shown in Fig. 10.

The impact of the split ratio on power density and efficiency is shown in Fig. 11. A quadratic impact on the power density can be observed as well as a saturation effect on efficiency. The special feature of the split ratio is that it cannot be chosen arbitrarily but is rather determined by the outer diameter. Split ratios chosen too high result in a low power density, as shown in Fig. 12 and Fig. 17 (Model D6). For smaller diameters, only a lower split ratio can be realized.

In Fig. 12, it can be seen that there is a specific section where both, power density and efficiency, can be improved. Beyond a maximum, efficiency increases at the cost of power density. With this behavior, it makes the split ratio the parameter that is most important to vary.

To select a value for the split ratio, a function was derived from the data of the average split ratio of the motors with highest power density and highest efficiency. Fig. 13 shows the result. The function for the split ratio

$$i(D_{a,1}) = -50 \cdot \left(\frac{D_{a,1}}{\text{mm}}\right)^{-1.05} + 0.98 \qquad (29)$$

depending on the outer diameter can also be used for higher diameters as shown in the figure. A limitation due to manufacturing possibilities is expected in the range of 0.93 and 0.95.

For further investigations, one electric motor of each diameter was selected for a good ratio of efficiency and power density. In Fig. 14, the whole data set and the selected models are shown.

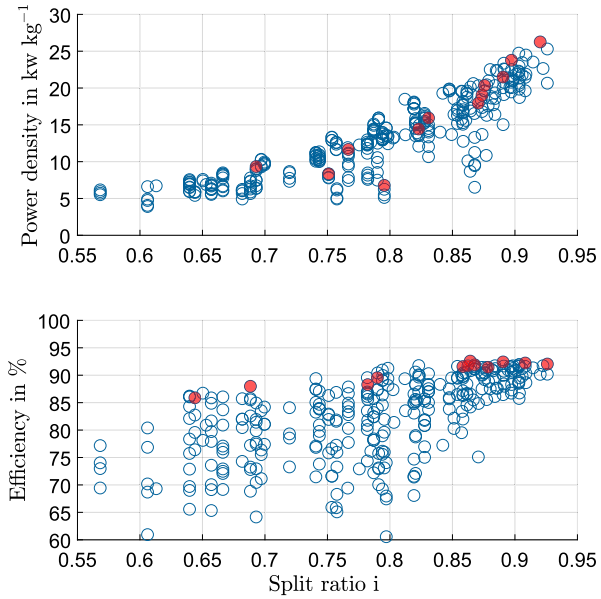

FIGURE 11. Impact of the split ratio *i* on the power density and efficiency. The red dots show the maximum power density and efficiency at the corresponding diameter.

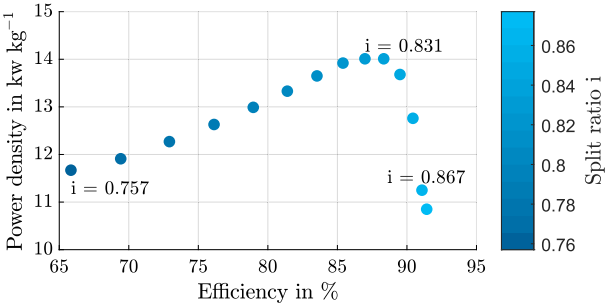

FIGURE 12. Variation of the split ratio i at a fixed outer diameter.

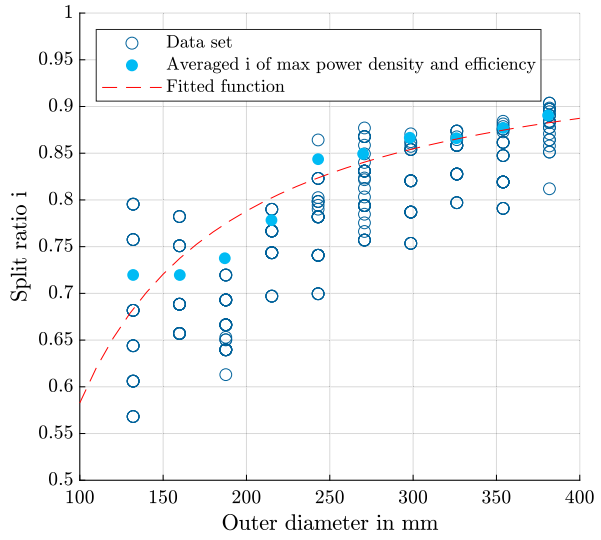

FIGURE 13. Guideline for the selection of the split ratio i depending on the outer diameter $D_{a,1}$.

Because all motors are sized for the same power, the motors are disproportionately long for small diameters and

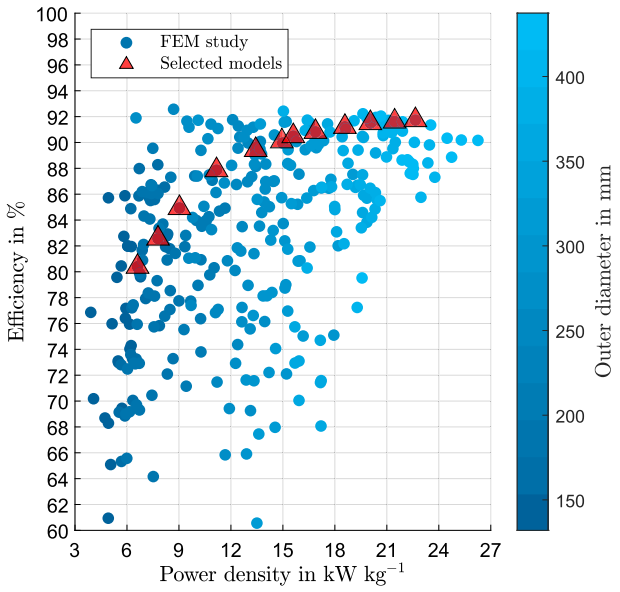

FIGURE 14. Power density and efficiency of all motor models.

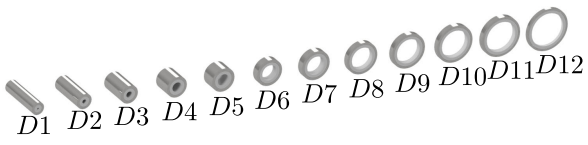

FIGURE 15. Comparison of the stator geometries of the selected models D1 to D12.

disproportionately short for large diameters. Figure 15 gives an insight into the stator geometry of the selected models.

Extreme values of diameter and length are characterized by different challenges. The small diameter and long length of the stator core make it difficult to cool the conductors. The cooling fluid reaches its maximum temperature along the length, and larger cooling channels are needed to compensate for this. This leads to a lower copper fill factor and thus to a lower efficiency. A large diameter and short active length means that end-winding effects become more significant and the torque calculated using the 2D FEM no longer corresponds to the real torque. In FEM the leakage inductance of the winding was considered but the leakage of the permanent magnet flux in the axial direction is missing. In order to gain an insight into this, a 3D FEM calculation was carried out. This was set up on the basis of the model D7. Another method is to consider this effect with the help of a lumped magnetic circuit like shown in [26] and [27]. From the 3D simulations, an adjustment function (Fig. 16) was derived, which was constructed by means of a diameter-to-length ratio. With this function, it is possible to calculate the torque reduction that occurs in a prototype that was developed in [22] and documented in a project report in [28]. However this function is not yet a sophisticated approach for describing the effect and requires more in-depth work. Nevertheless,

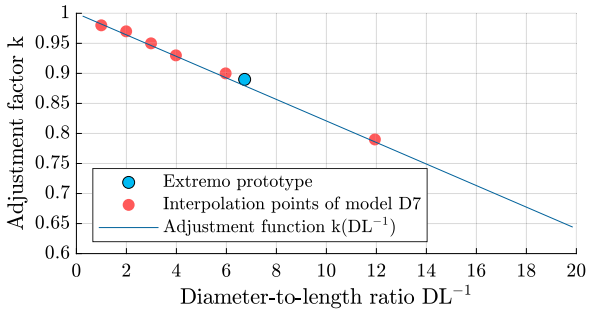

FIGURE 16. Torque adjustment function depending on the diameter-to-length ratio of the electric motor.

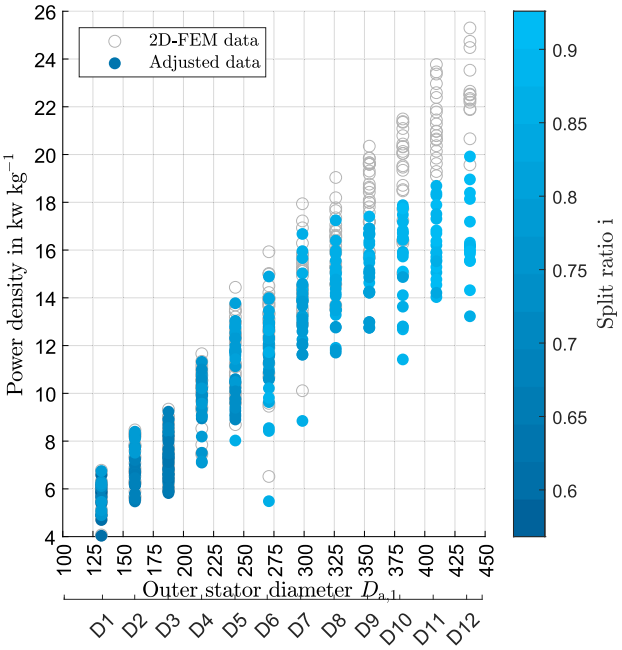

FIGURE 17. Power density and adjusted power density.

the adjustment function will be used to give an insight into influence of this effect on power density.

The adjustment function was applied to the power density data set. As shown in Fig. 17, larger diameters are more strongly affected by the end-winding effects, resulting in an optimum for power density.

VII. EVALUATION OF COMBINED PERFORMANCE OF ELECTRIC MOTOR AND PROPELLER

For the assessment of the combination of electric motor and propeller, the overall system mass needs to be considered. The mass of the motor m_{motor} of different diameter configurations, the number of propulsion units k, the power depending on the flight segment $P(t)$, the time t, the efficiency of the motor configurations in the context of a performance map $\eta_{\text{motor}}(P)$, the efficiency of the propeller configurations optimized for the flight mission $\eta_{\text{prop}}(P)$ and the energy density of the battery W_{bat} lead to the overall mass

$$m = k\left(m_{\text{motor}} + P(t)\cdot t\cdot \frac{1}{\eta_{\text{motor}}(P)\cdot\eta_{\text{prop}}(P)}\cdot W_{\text{bat}}\right) \tag{30}$$

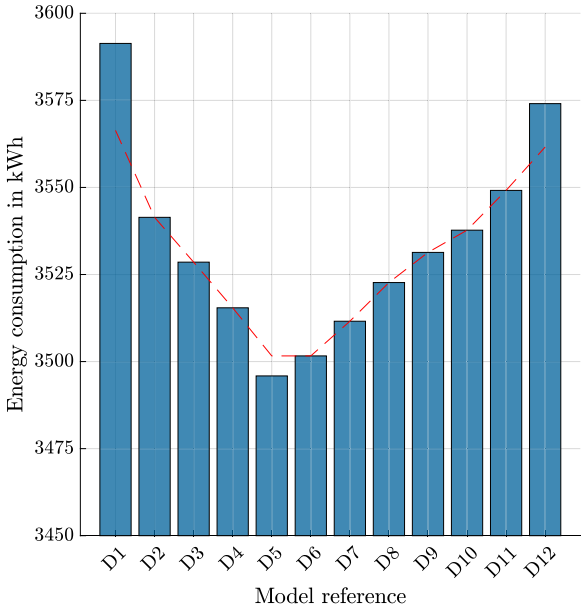

FIGURE 18. Energy consumption of the drive configurations D1 to D12.

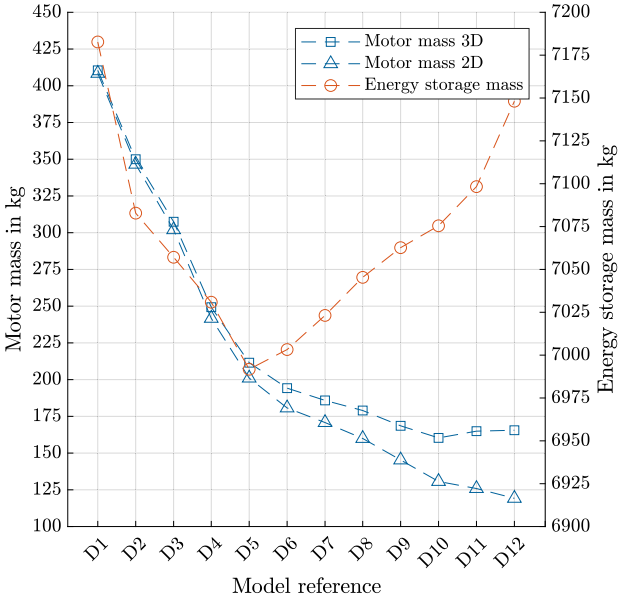

FIGURE 19. Comparison of the electric motor and the energy storage masses required for the given flight mission using the models D1 to D12.

of the system. Here, it is particularly important to emphasize how significant the influences of energy storage and flight duration are on the sizing of the propulsion system. Since the main objective of the study is the diameter and thus the available installation space, the data is presented with this focus.

The energy consumption was calculated according to the second part of Equation 30 and is shown in Fig. 18. A minimum can be found in the D5 configuration, which seems counterintuitive at first, since the efficiency of electric motors with larger diameters is higher (Fig. 14). The propellers with larger diameters require a slightly higher

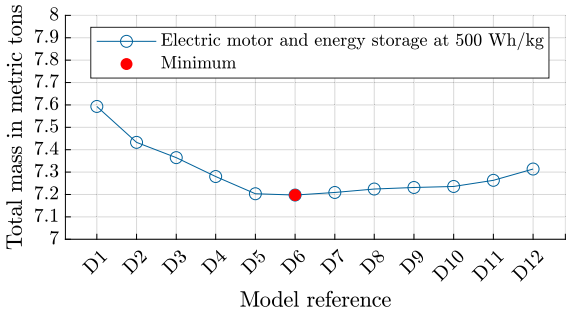

FIGURE 20. Combination of motor and energy storage mass at an energy density of 500 Wh/kg.

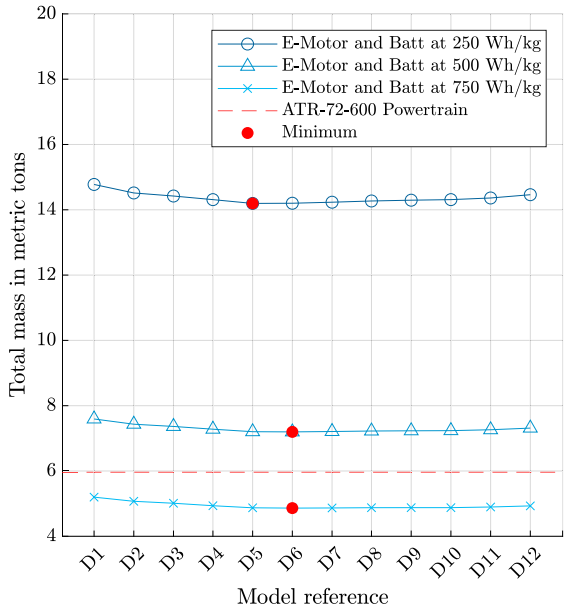

FIGURE 21. Overall mass of the powertrain at different energy densities compared to the ATR-72-600 powertrain.

power to fulfill the requirements of the flight mission and also have a lower efficiency and therefore lead to higher energy consumption.

Since the mass of the electric motor is the other part of the equation, the mass of the motor and the energy storage is evaluated and shown in Fig.19. The mass of the propeller was not considered, as the change in hub size does not result in a significant change in mass; this is because the propeller blades become shorter with increasing hub diameter, while the propeller diameter remains constant. The energy storage mass was calculated based on an energy density of 500 Wh/kg. The minimum can be observed for the model D5. The minimum of the motor mass is located at the larger diameters of D10 to D12. It is also shown how increasing the length of the electric motor to compensate for the end-region effects increases the motor mass.

The combination of motor and energy storage mass for the flight mission is shown in Fig. 20. It can be seen that a minimum occurs for the model D6. The differences between the models D5 to D7 are very small. Therefore, derived from the investigations, a hub-to-tip ratio of $\nu = 0.16$ to 0.20 is recommended. The installation space for an electric motor for a propeller is therefore defined as

$$D_{\mathrm{a},1} = D_{\mathrm{p}} \cdot \nu. \tag{31}$$

In order to emphasize the importance of the specific energy density of the energy storage, the mass of the overall system is shown in Fig. 21 for different specific energy densities. From Fig. 21, it can be seen that, while the specific energy density changes, the minimum of the overall system mass remains approximately at the same diameter.

VIII. CONCLUSION

In this publication, the combination of electric motor and propeller has been investigated. The main findings are:

- In this combination, there are two ways to optimize: an optimization with pitch angle and speed to maximize efficiency, or an optimization using the hub diameter which opens up the installation space for the electric motor.
- Optimization using pitch angle and speed can be done without the electric motor, since the efficiency of the propeller is dominant.
- The optimization of the hub diameter and outer diameter of the electric motor yields an optimum hub-to-tip ratio of 0.16 to 0.20.
- The reduction of the hub diameter is limited by electric motors with a rather long active length and therefore with lower power density and efficiency
- The expansion of the hub diameter is limited by electric motors with a rather short active length and therefore end-region effects are disproportionately pronounced and reduce the advantages.
- The split ratio was identified as one of the parameters with the biggest impact on power density and efficiency.
- A simplified equation for the selection of the split ratio matched to an outer diameter is given.
- A simplified equation for considering end-region effects is presented to avoid the need for time-consuming 3D FEM simulations
- Starting values and a description of the ratios of tooth width to slot width and tooth width to yoke height are given to narrow down the parameter space for the design of electric motors for aircraft propulsion.

ACKNOWLEDGMENT

The authors would like to thank the Open Access Publication Funds of Leibniz University Hannover.

REFERENCES

[1] A. M. Stoll, J. Bevirt, M. D. Moore, W. J. Fredericks, and N. K. Borer, *Drag Reduction Through Distributed Electric Propulsion*. Reston, VI, USA: American Institute of Aeronautics and Astronautics, 2014.
[2] S. Sahoo, X. Zhao, and K. Kyprianidis, "A review of concepts, benefits, and challenges for future electrical propulsion-based aircraft," *Aerospace*, vol. 7, no. 4, p. 44, Apr. 2020. [Online]. Available: https://www.mdpi.com/2226-4310/7/4/44
[3] S. Karpuk and A. Elham, "Influence of novel airframe technologies on the feasibility of fully-electric regional aviation," *Aerospace*, vol. 8, no. 6, p. 163, Jun. 2021. [Online]. Available: https://www.mdpi.com/2226-4310/8/6/163
[4] J. J. Berton and D. M. Nark, "Low-noise operating mode for propeller-driven electric airplanes," *J. Aircr.*, vol. 56, no. 4, pp. 1708–1714, Jul. 2019.

[5] S. Xiang, Y. Q. Liu, G. Tong, W. P. Zhao, S. X. Tong, and Y. D. Li, "An improved propeller design method for the electric aircraft," *Aerosp. Sci. Technol.*, vol. 78, pp. 488–493, 2018. [Online]. Available: https://www.sciencedirect.com/science/article/pii/S1270963818300270

[6] O. Gur and A. Rosen, "Optimization of propeller based propulsion system," *J. Aircr.*, vol. 46, no. 1, pp. 95–106, Jan. 2009.

[7] I. Bouzidi, A. Masmoudi, and N. Bianchi, "Electromagnetic/thermal design procedure of an aerospace electric propeller," in *Proc. 10th Int. Conf. Ecological Vehicles Renew. Energies (EVER)*, Mar. 2015, pp. 1–9.

[8] S. Cui, P. Sun, Z. Kuang, and T. Zhao, "A thermal-electromagnetic coupled motor design flow for electric aircraft propeller drive application," in *Proc. IEEE Transp. Electrific. Conf. Expo, Asia–Pacific (ITEC Asia-Pacific)*, Aug. 2017, pp. 1–6.

[9] A. Varyukhin, M. Ovdienko, V. Vavilov, A. Zherebtsov, I. Sayakhov, and G. Zinnatullina, "Research and development of a fault-tolerant small-sized electric motor for an aircraft propeller," in *Proc. Int. Conf. Electrotechnical Complexes Syst. (ICOECS)*, Nov. 2021, pp. 616–619.

[10] D. Golovanov, D. Gerada, Z. Xu, C. Gerada, A. Page, and T. Sawata, "Designing an advanced electrical motor for propulsion of electric aircraft," in *Proc. AIAA/IEEE Electric Aircr. Technol. Symp. (EATS)*, Aug. 2019, pp. 1–12.

[11] X. Zhang, C. L. Bowman, T. C. O'Connell, and K. S. Haran, "Large electric machines for aircraft electric propulsion," *IET Electric Power Appl.*, vol. 12, no. 6, pp. 767–779, Jul. 2018.

[12] K. Takahashi, H. Fujimoto, Y. Hori, H. Kobayashi, and A. Nishizawa, "Modeling of propeller electric airplane and thrust control using advantage of electric motor," in *Proc. IEEE 13th Int. Workshop Adv. Motion Control (AMC)*, Mar. 2014, pp. 482–487.

[13] S. Wang, S. Zhang, and S. Ma, "An energy efficiency optimization method for fixed pitch propeller electric aircraft propulsion systems," *IEEE Access*, vol. 7, pp. 159986–159993, 2019.

[14] B. Zaghari, A. Kiran, T. Sinnige, E. Pontika, H. B. Enalou, T. Kipouros, and P. Laskaridis, "The impact of electric machine and propeller coupling design on electrified aircraft noise and performance," in *Proc. AIAA SCITECH Forum*. Reston, VI, USA: American Institute of Aeronautics and Astronautics, 2023, pp. 1–9.

[15] T. Marien, N. J. Blaesser, Z. J. Frederick, M. D. Guynn, J. Kirk, K. Fisher, S. Schneider, R. P. Thacker, and P. Frederic, "Methodology used for an electrified aircraft propulsion design exploration," in *Proc. AIAA AVIATION FORUM*. Reston, VI, USA: American Institute of Aeronautics and Astronautics, 2021, p. 2017.

[16] T. Balachandran, J. David Reband, J. Xiao, S. Sirimmana, R. Dhilon, and K. S. Haran, "Co-design of an integrated direct-drive electric motor and ducted propeller for aircraft propulsion," in *Proc. AIAA/IEEE Electric Aircr. Technol. Symp. (EATS)*, Aug. 2020, pp. 1–11.

[17] T. Balachandran, J. Reband, M. Lewis, and K. S. Haran, "Co-design of integrated propeller and inner rotor PMSM for electric aircraft application," in *Proc. IEEE Int. Electric Mach. Drives Conf. (IEMDC)*, May 2021, pp. 1–8.

[18] C. N. Adkins and R. H. Liebeck, "Design of optimum propellers," *J. Propuls. Power*, vol. 10, no. 5, pp. 676–682, Sep. 1994.

[19] S. Lück, J. Göing, T. Wittmann, B. Kirsch, L. Benjamin, and J. Friedrichs, "Propeller design and performance evaluation with partially prescribed velocity distribution," in *Proc. Global Power Propuls. Soc. (GPPS)*, 2022, pp. 1–5.

[20] G. Müller and B. Ponick, *Theorie Elektrischer Maschinen*, vol. 3, 6th ed. Weinheim, Germany: Wiley-VCH, 2009.

[21] T. Finken, *Fahrzyklusgerechte Auslegung von Permanentmagneterregten Synchronmaschinen für Hybrid- und Elektrofahrzeuge* (Aachener Schriftenreihe zur Elektromagnetischen Energiewandlung), vol. 11. Aachen, Germany: Shaker, 2011.

[22] C. M. Wohlers, *Permanenterregte Synchronmaschinen Hoher Drehmomentdichte* (Berichte Aus Dem IAL), vol. 4. Garbsen, Germany: Tewiss, 2021.

[23] C. Wohlers and B. Ponick, "First estimations of stator dimensions for permanent magnet synchronous machines with tooth-coil windings and direct liquid cooling," in *Proc. Int. Conf. Electr. Mach. (ICEM)*, vol. 1, Aug. 2020, pp. 462–468.

[24] C. Wohlers, P. Juris, S. Kabelac, and B. Ponick, "Design and direct liquid cooling of tooth-coil windings," *Electr. Eng.*, vol. 100, pp. 2299–2308, Dec. 2018.

[25] A. Binder, *Elektrische Maschinen und Antriebe*, 2nd ed. Berlin, Germany: Springer Vieweg, 2018.

[26] J.-M. Seo, A.-R. Ro, R.-E. Kim, and J. Seo, "Hybrid analysis method considering the axial flux leakage in spoke-type permanent magnet machines," *IEEE Trans. Magn.*, vol. 56, no. 9, pp. 1–6, Sep. 2020.

[27] C.-H. Seok, S.-Y. Yoon, H.-S. Choi, H.-Y. Lee, and J. Seo, "Analysis and modeling of axial leakage for spoke-type hybrid permanent magnet machines," *IEEE Access*, vol. 11, pp. 6385–6393, 2023.

[28] C. Wohlers, M. Hempel, and A. A. Johnson. (2023). *Elektroantriebe Mit Extremer Drehmomentdichte: Forschungsbericht, Fva 800 I IGF-Nr. 19578-N*. [Online]. Available: https://fva-net.de/aktuelles/detail/elektroantriebe-mit-extremer-drehmomentichte-525/

RALF JOHANNES KEUTER (Graduate Student Member, IEEE) was born in Meppen, Germany, in August 1990. He received the dual bachelor's degree in engineering of technical systems and an apprenticeship as an electrician for machines and drive technology from the Osnabrück University of Applied Science, Lingen, in 2014, and the master's degree in electrical engineering from Leibniz University Hannover, in 2018. After finishing the dual bachelor's studies, he is an Electrical Design Engineer on induction machines for customized machines and hoisting machinery with Franz Wölfer Elektromaschinenfabrik Osnabrück. After finishing the master's study, he is currently a Research Associate with the Institute for Drive Systems and Power Electronics, Leibniz University Hannover.

BASTIAN KIRSCH was born in Fulda, Germany, in 1992. He received the M.Sc. degree in aerospace engineering from the University of Stuttgart, in 2018. Since April 2018, he has been a Research Assistant with the Institute of Jet Propulsion and Turbomachinery, Technische Universität Braunschweig, where he is involved in the interaction between propeller and wing for distributed propulsion.

JENS FRIEDRICHS received the Ph.D. degree in mechanical engineering from Technische Universität Braunschweig (TU Braunschweig), in 2002. Then, he held various positions with MTU Maintenance Hannover GmbH in engineering and most recently as the Programme Director GE CF6. In 2010, he returned to TU Braunschweig as a Professor of aircraft propulsion systems, where he is the Director of the Institute of Aircraft Propulsion Systems and Turbomachinery (IFAS). From 2015 to 2017, he was the Dean of the Faculty of Mechanical Engineering, TU Braunschweig. Since 2019, he has been a Spokesperson with the SE^2A–Sustainable and Energy Efficient Aviation Excellence Cluster, TU Braunschweig, which, together with its partners Leibniz University Hannover, DLR, PTB, and HBK, is focusing on fundamental research for future sustainable aviation.

BERND PONICK was born in Großburgwedel, Germany, in 1964. He received the Dipl.-Ing. degree in electrical power engineering from the University of Hannover, in 1990, and the Dr.-Ing. degree in electrical machines, in 1994. After nine years with the Large Drives Division, Siemens, as a Design Engineer, for large variable speed motors, the Head of Electrical Design, and the Technical Director of Siemens AG Dynamowerk Berlin. Since 2003, he has been a Full Professor of electrical machines and drive systems with Leibniz University Hannover. His main research interests include calculation and simulation methods for electrical machines, prediction of and measures to mitigate important parasitic effects, such as magnetic noise, additional losses or bearing currents, and new applications for electrical machines, such as electric and hybrid vehicles.